Adjoint inverse modeling of black carbon during the Asian Pacific Regional Aerosol Characterization Experiment

A. Hakami, D. K. Henze, and J. H. Seinfeld

Departments of Chemical Engineering and Environmental Science and Engineering, California Institute of Technology, Pasadena, California, USA

T. Chai, Y. Tang, and G. R. Carmichael

Center for Global and Regional Environmental Research, University of Iowa, Iowa City, Iowa, USA

A. Sandu

Department of Computer Science, Virginia Polytechnic Institute and State University, Blacksburg, Virginia, USA

Received 7 December 2004; revised 24 March 2005; accepted 8 April 2005; published 19 July 2005.

[1] An adjoint model is used for inverse modeling of black carbon during the Asian Pacific Regional Aerosol Characterization Experiment (ACE-Asia). We use the four-dimensional variational data assimilation (4D-Var) approach to optimally recover spatially resolved anthropogenic and biomass-burning emissions and initial and boundary conditions of black carbon. Boundary conditions and biomass-burning emissions are assigned daily scaling factors. Anthropogenic emissions are scaled by a combination of daily and monthly scaling factors. Simulation results are compared to various observations of black carbon concentrations during the campaign. Measurements at five islands and on board the research vessel *Ronald H. Brown* are used for inverse modeling. Different levels of constraints are examined for inversion, and a case with 62% reduction in the total square errors is chosen. The assimilated results are compared with the observations on board the Twin Otter aircraft that were not used for assimilation. Among the scaled variables, anthropogenic emissions are the most significant, followed by the boundary conditions. The domain-wide emissions inventory does not change significantly as a result of the assimilation, but sizable changes occur on the subregional level. Most noticeably, anthropogenic emissions over southeastern China are reduced while those in northeast China and Japan are increased.

Citation: Hakami, A., D. K. Henze, J. H. Seinfeld, T. Chai, Y. Tang, G. R. Carmichael, and A. Sandu (2005), Adjoint inverse modeling of black carbon during the Asian Pacific Regional Aerosol Characterization Experiment, *J. Geophys. Res.*, *110*, D14301, doi:10.1029/2004JD005671.

1. Introduction

[2] Black (or elemental) carbon (BC) is the main light absorbing aerosol species; it alters the radiative properties of other aerosols with which it is mixed, and it may affect cloud formation and precipitation. In short, understanding the regional and global distributions of BC is key to predicting the effect of aerosols on global and regional climate. A number of investigators have simulated top of the atmosphere (TOA) direct radiative forcing of black carbon, values of which range from approximately +0.1 to +0.8 W/m^2 [*Haywood and Shine*, 1995; *Haywood et al.*, 1997; *Haywood and Ramaswamy*, 1998; *Penner et al.*, 1998; *Myhre et al.*, 1998; *Cooke et al.*, 1999; *Jacobson*, 2001, 2002; *Koch*, 2001; *Chung and Seinfeld*, 2002; *Wang*, 2004]. The wide range of estimates is primarily a result of different assumptions about the mixing state of BC with sulfate aerosols and of the global burden of BC. A significant source of uncertainty in the estimates is the BC emissions inventory itself. Global and regional emission inventories of BC have been refined [*Cooke and Wilson*, 1996; *Liousse et al.*, 1996; *Cooke et al.*, 1999; *Streets et al.*, 2003a; *Bond et al.*, 2004; *Schaap et al.*, 2004]; nevertheless, emissions uncertainty remains a significant contributor to the overall uncertainty in predicted global BC distributions. These uncertainties play an even more significant role in regional/episodic simulations, where the actual emissions are more likely to deviate from the annual mean inventory. Regional studies present a particularly advantageous opportunity to evaluate our understanding of the relationship between observed BC levels and existing emissions inventories. Furthermore, owing to its relatively short atmospheric lifetime (4–10 days), BC emissions have their most pronounced effect on the regional scale.

[3] Inverse modeling provides a powerful approach for observation-based inference about atmospheric model inputs (e.g., emissions). Methods based on the Kalman

0148-0227/05/2004JD005671$09.00

filter and its variations assume an imperfect (noisy) model and are able to propagate the error characteristics through the formalism of the method. Kalman filtering has been widely applied to meteorological and atmospheric data assimilation problems [*Menard et al.*, 2000; *Khattatov et al.*, 2000]. Methods based on the Kalman filter tend to be computationally demanding and therefore have seen limited use in large-scale atmospheric chemical transport models (CTMs) [*Mulholland and Seinfeld*, 1995; *Houtekamer and Mitchell*, 1998; *van Loon et al.*, 2000]. Alternatively, adjoint modeling [*Marchuk*, 1974, 1986; *Cacuci*, 1981] can be used to calculate gradients of an objective function with respect to model input parameters. In adjoint analysis, the model is considered as a strong constraint for the problem; that is, the model is assumed to be perfect. Adjoint data assimilation [*Talagrand*, 1981a, 1981b; *Le Dimet and Talagrand*, 1986; *Talagrand and Courtier*, 1987] has been used in meteorology and oceanography [*Courtier and Talagrand*, 1987; *Navon*, 1997; *Usbeck et al.*, 2003].

[4] In the context of three-dimensional (3-D) Eulerian CTMs, adjoint modeling offers an efficient method for inverse modeling applications, as desired gradients of the objective function are calculated simultaneously. *Elbern and Schmidt* [1999] applied the adjoint method to the European air pollution dispersion chemical transport model 2 (EURAD-CTM2) for data assimilation. They present a variety of identical twin experiments to verify the adjoint implementation; most notably they were able to recover initial concentrations of NO_x and VOC from ground level ozone observations. In an identical twin experiment, the simulation results for a perturbed set of parameters are used as observations, and the adjoint analysis is used to recover the applied changes in parameters. The advantage of the identical twin experiment is that the true answer to the inverse problem is known. *Elbern et al.* [2000] used the same model and methodology for recovery of NO_x and VOC emission rates from ozone observations. *Vukicevic and Hess* [2000] implemented adjoint modeling in HANK, a chemical transport model based on MM5 meteorological outputs. The sensitivity of hypothetical soluble and insoluble species concentrations at Hawaii with respect to a variety of different model parameters was calculated. *Vautard et al.* [2000] apply an adjoint version of the chemical transport model CHIMERE [*Menut et al.*, 2000] using ozone observations for recovery of urban boundary ozone values. *Elbern and Schmidt* [2001] used EURAD-CTM2 and applied four-dimensional variational (4D-Var) data assimilation to an ozone episode over central Europe to optimize various initial concentrations. *Schmidt and Martin* [2003] and *Menut* [2003] applied the adjoint technique in CHIMERE for episodic sensitivity analysis. *Sandu et al.* [2005] formulate continuous and discrete adjoints for implementation in chemical kinetic systems [*Sandu et al.*, 2003] and 3-D air quality models. They apply the method in the chemical transport model STEM-2k1 [*Carmichael et al.*, 2003b] for sensitivity analysis and recovery of various initial conditions in identical twin experiments.

[5] Here, we adapt an adjoint model of the chemical transport model STEM-2k1 [*Carmichael et al.*, 2003b; *Sandu et al.*, 2005] for assimilating BC concentrations and recovery of its emissions (anthropogenic and biomass burning), boundary conditions, and initial conditions in eastern Asia during the Asian Pacific Regional Aerosol Characterization Experiment (ACE-Asia) field study [*Huebert et al.*, 2003; *Seinfeld et al.*, 2004]. East and Southeast Asia are major contributors to the total global BC burden [*Bond et al.*, 2004], and the ACE-Asia campaign provides a unique opportunity to better constrain these emissions. Our goal is to employ BC measurements carried out during ACE-Asia (April 2001) to optimally estimate east Asian BC emissions (and initial and boundary conditions). The long assimilation window is essential for regional inverse modeling, where long-range transport of pollutants becomes important. Assimilation is based on direct observations of BC aerosol mass concentrations in four Japanese islands along ~140°E longitude, Gosan, South Korea, and on board R/V *Ronald H. Brown*.

2. Adjoint Formulation

[6] The equation governing the dynamics of a chemically nonreactive species (e.g., BC) in atmospheric CTMs is [*Seinfeld and Pandis*, 1998; *Jacobson*, 1998]

$$\frac{\partial C}{\partial t} = -\nabla \cdot (\mathbf{u}C) + \nabla \cdot (\mathbf{K}\nabla C) + E - k_w C \tag{1}$$

where C is the concentration of the species, $\mathbf{u}$ is the vector wind field, and $\mathbf{K}$ is the diffusivity tensor. E represents elevated emissions, and k_w is the first-order rate constant for wet removal of the species. Equation (1), which in inverse modeling is referred to as the forward model, is solved subject to specific initial and boundary conditions; while the formulation of these conditions may vary slightly from one CTM to another, they invariably contain similar key input parameters. For STEM, the initial conditions, surface boundary condition, and lateral inflow boundary conditions are [*Sandu et al.*, 2005]

$$\begin{aligned} &C(\omega, t_0) = C^0(\omega) \\ &C(\omega, t)|_{\omega\in\Gamma^{in}} = C^b(\omega, t) \\ &K\frac{\partial C}{\partial \omega}|_{\omega\in\Gamma^{out}} = 0 \\ &\left(K\frac{\partial C}{\partial \omega} - v_d C + E^0\right)|_{\omega\in\Gamma^{gr}} = 0 \end{aligned} \tag{2}$$

where ω is a generalized spatial coordinate vector, C^0 and C^b are the initial and boundary concentrations, respectively, and Γ represents the boundary cells (inflow, outflow, or ground level); v_d is the species dry deposition velocity, and E^0 is its surface-level emission rate.

[7] In adjoint sensitivity analysis, the gradients of a scalar function J with respect to a set of input parameters are calculated. For data assimilation applications, this scalar takes the form of an objective (cost) function, and is generally defined as

$$J(\mathbf{C}, \boldsymbol{\alpha}) = \frac{1}{2}\left[\frac{1}{\mu}\int_{t_0}^{t_F} (\boldsymbol{\alpha}^{\mathbf{b}} - \boldsymbol{\alpha})^{\mathbf{T}} \mathbf{N}^{-1} (\boldsymbol{\alpha}^{\mathbf{b}} - \boldsymbol{\alpha}) + \int_{t_0}^{t_F} (\hat{\mathbf{C}} - \mathbf{C})^{\mathbf{T}} \mathbf{R}^{-1} (\hat{\mathbf{C}} - \mathbf{C})\right] \tag{3}$$

where $\hat{\mathbf{C}}$ and $\mathbf{C}$ are vectors of the observed and simulated concentrations (temporal and spatial dependences are omitted for simplicity), respectively. t_0 and t_F are the initial and final times of the simulation; $\boldsymbol{\alpha}$ denotes the set of input parameters that are to be optimally estimated in the assimilation, and $\boldsymbol{\alpha}^{\mathbf{b}}$ is the vector of initial (background) estimates for those parameters. Uncertainty in the data and inputs is incorporated into the objective function through the error covariance matrices for the observations and inputs, $\mathbf{R}$ and $\mathbf{N}$, respectively. In so doing, observations or a priori estimates with high uncertainty have a lower contribution to the overall objective function. μ is a global weighting factor (a regularization parameter) for assigning relative emphases on either the observations or background values (discussed later in the text). The objective function is evaluated for grid cells and times where observations are available. For uncorrelated errors and discrete temporal and spatial observations, the scalar objective function can be written as

$$J = \frac{1}{2}\left[\frac{1}{\mu}\sum_k N_k^{-1}\left(\alpha_k^b - \alpha_k\right)^2\right] + \frac{1}{2}\left[\sum_i\sum_j R_{ij}^{-1}\left(\hat{C}_{ij} - C_{ij}\right)^2\right] \tag{4}$$

where indices i and j represent the time and location of the observations, and index k represents the particular parameter to be estimated.

[8] A perturbation in the input parameters, $\delta\boldsymbol{\alpha}$, translates into perturbations in the simulated concentrations and the cost function, $\delta\mathbf{C}$ and δJ. Applying a Lagrange multiplier λ to the perturbed form of equation (3) (and assuming uncorrelated observation errors) results in [*Marchuk*, 1986; *Vukicevic and Hess*, 2000; *Elbern et al.*, 2000; *Sandu et al.*, 2005]

$$\begin{aligned}\delta J = &\frac{1}{\mu}\int_t \left(\boldsymbol{\alpha} - \boldsymbol{\alpha}^{\mathbf{b}}\right)^{\mathbf{T}}\mathbf{N}^{-1}\delta\boldsymbol{\alpha}dt + \int_t\int_\Omega \phi(\omega,t)\delta C d\omega dt\\ &- \int_t\int_\Omega \lambda\left(\frac{\partial\delta C}{\partial t} + \nabla\cdot(\mathbf{u}\delta C)\right.\\ &\left.-\nabla\cdot(\mathbf{K}\nabla\delta C) - \delta E + k_w\delta C\right)d\omega dt\end{aligned} \tag{5}$$

where $\phi(\omega, t) = [(C - \hat{C})/R(\omega, t)]$ is the observation-driven forcing term for the adjoint system. After integration by parts and rearrangement, the following equation can be used to calculate the time- and location-dependent gradients of the cost function

$$\begin{aligned}\frac{\delta J}{\delta\boldsymbol{\alpha}_{\mathbf{I}}}(\omega,t) &= \frac{1}{\mu}\mathbf{N}^{-1}\left(\boldsymbol{\alpha}_{\mathbf{I}} - \boldsymbol{\alpha}_{\mathbf{I}}^{\mathbf{b}}\right) + \lambda|_{t=0}\\ \frac{\delta J}{\delta\boldsymbol{\alpha}_{\mathbf{B}}}(\omega^b,t) &= \frac{1}{\mu}\mathbf{N}^{-1}\left(\boldsymbol{\alpha}_{\mathbf{B}} - \boldsymbol{\alpha}_{\mathbf{B}}^{\mathbf{b}}\right) + \left(\mathbf{u}\lambda|_{\omega\in\Gamma^{in}} + K\frac{\partial\lambda}{\partial\omega}|_{\omega\in\Gamma^{in}}\right)\\ \frac{\delta J}{\delta\boldsymbol{\alpha}_{\mathbf{E}}}(\omega,t) &= \frac{1}{\mu}\mathbf{N}^{-1}\left(\boldsymbol{\alpha}_{\mathbf{E}} - \boldsymbol{\alpha}_{\mathbf{E}}^{\mathbf{b}}\right) + \lambda\\ \frac{\delta J}{\delta\boldsymbol{\alpha}_{\mathbf{E}^0}}(\omega^{gr},t) &= \frac{1}{\mu}\mathbf{N}^{-1}\left(\boldsymbol{\alpha}_{\mathbf{E}^0} - \boldsymbol{\alpha}_{\mathbf{E}^0}^{\mathbf{b}}\right) + \lambda|_{\omega\in\Gamma^{gr}}\end{aligned} \tag{6}$$

provided that λ, the adjoint variable for the concentration, satisfies the following adjoint equation

$$-\frac{\partial\lambda}{\partial t} = \nabla\cdot(\mathbf{u}\lambda) + \nabla\cdot(\mathbf{K}\nabla\lambda) - k_w\lambda + \phi(\omega,t) \tag{7}$$

subject to the following conditions:

$$\begin{aligned}&\lambda(t_F) = 0\\ &\lambda|_{\omega\in\Gamma^{out}} = 0\\ &K\frac{\partial\lambda}{\partial\omega}|_{\omega\in\Gamma^{out}} = 0\\ &\left(K\frac{\partial\lambda}{\partial\omega} - v_d\lambda\right)|_{\omega\in\Gamma^{gr}} = 0\end{aligned} \tag{8}$$

$\boldsymbol{\alpha}_{\mathbf{I}}$, $\boldsymbol{\alpha}_{\mathbf{B}}$, $\boldsymbol{\alpha}_{\mathbf{E}}$, and $\boldsymbol{\alpha}_{\mathbf{E}^0}$ in equation (6) represent the initial conditions, boundary conditions, elevated emissions, and surface emissions, respectively. Note that the adjoint equation is driven by differences between observations and simulations (the forcing term ϕ). Note that the negative sign for the time derivative term in equation (7) indicates that the adjoint equation is integrated backward in time from t_F to t_0.

[9] Equation (7) and the initial and boundary conditions in equation (8) uniquely define the solution for the adjoint system. Once the adjoint is integrated backward in time, the gradients of the cost function can be calculated on the basis of equation (6). These equations are derived for the continuous equation (1) and must be solved numerically. Alternatively, one can derive the adjoint equation for the numerical (discretized) solution to equation (1). The two alternatives are not exactly equivalent, as the adjoint and discretization operations are not generally commutable [*Sirkes and Tziperman*, 1997; *Sandu et al.*, 2003]. The discrete gradient equation based on numerical algorithms used in STEM [*Sandu et al.*, 2005] can be written as

$$\begin{aligned}\delta J = &\frac{1}{\mu}\sum_t\sum_k f_k'\left(\frac{f_k - 1}{N_k}\right)\delta\varepsilon_k\\ &+ \sum_\Omega\left[C^0(\omega)\lambda(\omega,t^0)\right]\delta\varepsilon_I\\ &+ \sum_t\sum_{\Gamma^{gr}}\left[E^0(\omega^{gr},t)\lambda(\omega^{gr},t)\Delta t\right]\delta\varepsilon_{E^0}(\omega^{gr},t)\\ &+ \sum_t\sum_\Omega\left[E(\omega,t)\lambda(\omega,t)\Delta t\right]\delta\varepsilon_E(\omega,t)\\ &+ \sum_t\sum_{\Gamma^{in}}\left\{C^b(\omega^b,t)\left[\left(\frac{u(\omega^{b1},t)}{\Delta\omega} + \frac{K(\omega^{b1},t)}{\Delta\omega^2}\right)\right.\right.\\ &\left.\left.\cdot\lambda(\omega^{b1},t) - \frac{u(\omega^{b2},t)}{6\Delta\omega}\lambda(\omega^{b2},t)\right]\Delta t\right\}\delta\varepsilon_B(\omega^b,t)\end{aligned} \tag{9}$$

where ε represents an individual dimensionless scaling factor applied to each of the input parameters (distinguished by the subscripts), i.e., $\alpha_k = \varepsilon_k\alpha_k^b$. The function f_k is defined as $f_k = \max(\varepsilon_k, 1/\varepsilon_k)$ and f_k' is its derivative with respect to the individual scaling factor. This form of background-driven cost is used to assign equivalent penalties to scaling up or down from the background values. Superscripts b, $b1$, and $b2$ show the outside, first, and second stripe of interior boundary cells, respectively. For horizontal advection, a third-order upwind numerical scheme is used, hence the term for the second interior stripe in the boundary condition gradient. During the assimilation process each of the scaling factors (all of which have an initial value of one) is optimally estimated. By employing the scaling factors, the optimization process focuses on the input parameters with

larger magnitudes. Also, by optimizing for the scaling factors (rather than the real fields), all input parameters are uniformly represented in the cost function. Another advantage of using scaling factors is that input parameters with a magnitude of zero will not play a role in the optimization; for example, a grid cell with zero emissions (over the ocean) cannot have any emissions assigned to it as a result of the optimization. Alternatively, one may optimize the emissions only in the prescribed areas (i.e., excluding the ocean), and thus reducing the size and cost of the optimization problem.

3. Inverse Modeling of Black Carbon Over East Asia

[10] The objective of inverse modeling is to estimate the input parameters in order to achieve optimized model performance, i.e., to minimize the cost function. In the larger scheme, it is desirable to identify any existing biases and systematic errors in the input estimates. CTMs and general circulation models (GCMs) require a multitude of inputs, many of which are highly uncertain. Furthermore, most of such inputs vary in space and/or time. As a result, a large number of input parameters can be estimated in the assimilation process. As the available observations are usually scarce, atmospheric inverse modeling is often an extremely underdetermined problem.

[11] Equation (9) (or equation (6) for continuous form) allows for calculation of the gradient of the cost function with respect to any input parameter at any location and/or time. The 4-D adjoint analysis results in spatial and temporal distributions of the gradients of the objective function. These gradients directly link the objective function to the input parameters at different times and locations, taking into account all physical processes that are included in the model. In other words, adjoint results can be easily used to objectively identify locations and times that most affect model performance.

[12] The CTM used in this study is the adjoint version of STEM-2k1 [*Sandu et al.*, 2005; *Carmichael et al.*, 2003b], a parallel implementation of STEM using the communication and parallelization library of PAQMSG [*Miehe et al.*, 2002]. The model utilizes an operator-splitting scheme, and in the parallel mode breaks the computational domain into horizontal and vertical slices to be sent to available processors. For each time step, the required data (emissions, wind field, etc.) are gathered and processed by the master node, while computations are distributed among the worker nodes. The model uses efficient two-level checkpoint storage, as the state vector (concentrations) is required for the integration of the adjoint in nonlinear processes. However, as BC is chemically nonreactive, chemistry is not active and no checkpoint is required.

[13] The modeling domain for this study extends approximately between 10°N, 50°N, 90°E, and 155°E, as shown in Figure 1. The computational domain consists of 90 × 60 × 18 grid cells. Horizontal grid resolution is 80 km, and variable vertical spacing follows the topography of the terrain. The simulation period is the month of April 2001. Adjoint analysis and scaling is conducted for the monthlong assimilation window. The meteorological fields (winds, turbulence, precipitation, etc.) for STEM are produced by the mesoscale meteorological model RAMS [*Pielke et al.*, 1992]. Base case boundary conditions are taken to be time-invariant and for each altitude are set to the fifth percentile of all the observations during the TRACE-P measurements [*Carmichael et al.*, 2003b]. Boundary conditions for all lateral boundaries in each vertical layer are set to the same value, and the model does not account for time- and location-specific variabilities in lateral boundary conditions. Initial conditions are calculated from the simulations of the previous month (March 2001).

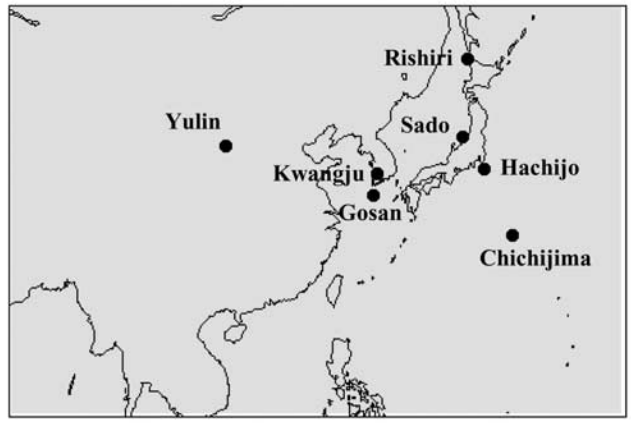

Figure 1. Modeling domain for the adjoint inverse modeling. Observation sites considered for assimilation are also shown.

[14] BC lifetime and concentrations can be strongly affected by precipitation if the BC occurs internally mixed with soluble species. The first-order wet removal constant is assumed to depend on the precipitation rate via the following empirical relation [*Uno et al.*, 2003a], $k_w = 10^{-5}\, h^{0.88}$, where k_w is the first-order removal rate constant (s^{-1}), and h is the precipitation rate, in mm h^{-1}. The constant (10^{-5}) is chosen on the basis of forward sensitivity analysis with respect to the magnitude of the constant such that the model overpredictions at four Japanese stations during the precipitation episodes are minimized, and it corresponds to ~20% of the value used for the wet removal of sulfate aerosols [*Uno et al.*, 2003a].

[15] The basic gridded BC emission inventory is based on the regional gaseous and aerosol primary emissions inventory for the year 2000 of *Streets et al.* [2003a, 2003b], specifically developed for support of the intensive field studies in the region, TRACE-P [*Jacob et al.*, 2003] and ACE-Asia. The inventory was prepared using a bottom-up approach and is based on energy consumption and activity information for various emission sectors: industrial, residential, transportation, power generation, agricultural, biomass burning (BB), and others. The biomass-burning inventory was prepared using vegetation cover maps, satellite fire count data, and a variety of other open fire information [*Woo et al.*, 2003]. The overall uncertainty in BC emissions (BB and other anthropogenic sources) is considered to be one of the largest among different species represented in the inventory. In different regions, total anthropogenic emissions and BB have a range of uncertainty (95% confidence interval) of 80–490%, and 200–700%, respectively. Over all of Asia, the uncertainties in anthro-

pogenic and BB emissions are estimated at about 360 and 450%, respectively [*Streets et al.*, 2003a].

[16] From an implementation point of view, BC emissions are separated into open BB and (other) anthropogenic emissions (i.e., fossil and biofuel). For biomass burning, the files contain the spatial distribution of the daily emissions. It is assumed that the rate of emission for each grid cell remains constant throughout the day. These daily values are then distributed into different vertical layers. The anthropogenic emissions are aggregated from different emission sectors (except BB) into one file. This input file contains gridded BC diurnal emissions (18 vertical layers) for a typical day in April 2001. Therefore the available emissions do not provide information on day-specific variability for anthropogenic BC, or on time-specific variability for BB emissions of BC. Furthermore, BB emission inputs do not account for location-specific variability in vertical profile of BC emissions. These limitations (in addition to that pertaining to boundary conditions) are relaxed in the time- and location-dependent scaling of input parameters through adjoint inverse modeling.

[17] Four different types of input parameters are scaled for BC assimilation: anthropogenic BC emissions (first 4 vertical layers in the boundary layer, time-dependent), biomass-burning BC emissions (first 12 vertical layers, time-dependent), lateral boundary conditions (18 layers, time-dependent), and initial conditions (18 layers). The scaling factors for biomass BC emissions and boundary BC concentrations are considered as daily averages, and their corresponding gradients are integrated over each day. Scaling factors for initial BC concentration are time independent. For anthropogenic BC emissions, the scaling factor is assumed to include a monthly portion (the gradient of which is integrated over the entire month), and a daily portion that is added to the monthly scaling factor. For all types of parameters, one scaling factor is assigned to each grid cell in the computational domain. The monthly and daily portions are assigned initial values of one and zero, respectively. The daily portion allows for limited day-to-day variability in the emissions for each grid cell. Assimilation and parameter optimization is an iterative procedure. A quasi-Newton limited memory optimization routine, L-BFGS [*Byrd et al.*, 1995], is used for optimization after each iteration. Four-dimensional (time and space) data assimilation results in a field of scaling parameters (3-D in case of initial conditions, and monthly anthropogenic BC emissions) following each iteration.

4. Black Carbon Observations During ACE-Asia

[18] During the ACE-Asia campaign, an extensive network of aircraft, shipboard, and surface instruments was utilized to measure different characteristics of the regional aerosols and their gaseous precursors. Observations included mass concentrations of BC, as well as frequent measurements of aerosol optical (absorption) properties, from which BC mass concentrations can be estimated.

[19] The success of any inverse modeling depends critically on the amount of data available for analysis. Since the three-dimensional adjoint equations are driven by the discrepancy between observations and simulation, greater spatial coverage (i.e., more observation sites) will significantly enhance the ability of the adjoints to capture the areas of influence on the objective function. In other words, comprehensive temporal and spatial coverage of observations provides the best opportunity for high-quality inversion. Whereas it was deemed important to include all the applicable BC observations in the analysis, it is also necessary to assign some measure of reliability to the available observations. Three main factors can contribute to the degree of importance of the observational data sets for inverse modeling:

[20] 1. Low uncertainty: In addition to the obvious case of measurement/sampling uncertainty, particular attention should be paid to the representativeness uncertainty, i.e., the uncertainty in representing a grid cell or computational node by a single point measurement.

[21] 2. High time resolution: Short-term observations produce more of an impulse perturbation in the adjoint variables than those that are averaged over a long time. In the latter case, underpredictions and overpredictions may cancel each other and result in loss of information in the adjoints. It should be noted, however, that very low sampling frequency (i.e., grab sampling) usually results in increased uncertainty.

[22] 3. Added spatial coverage: As mentioned above, more complete spatial coverage results in better representation of the adjoints, and in more information about the areas of influence. Therefore a low-quality data set in an otherwise undersampled location may be more important than higher-quality, but spatially redundant, observations. In addition, proximity of the observations to the more important parameters (e.g., emissions in a particular region) can be a significant advantage.

[23] For the current study, short-term BC mass measurements are the most suitable type of observations for inverse modeling. Mass concentrations deduced from optical measurements are inherently more uncertain, because of variability in the specific mass absorption efficiency [*Chuang et al.*, 2003; *Clarke et al.*, 2004], and are therefore considered less reliable and are not used in this study. The available BC measurements that are considered for this study are summarized in Table 1.

[24] The Variation of Marine Aerosol Properties (VMAP) network was designed for the estimation of latitudinal gradients of aerosols along the $\sim$140°E longitude, and provides the largest number of BC mass observations for the ACE-Asia. Another important set of observations is daily measurements at Gosan, as they were cross-examined with independent measurements at the station. The observations on board the research vessel (R/V) *Ron Brown* are also of particular interest, as they are sampled over a short period of time and are unaffected by direct emission sources.

[25] We compare all the observations listed in Table 1 with the model predictions. BC measurements at Gosan, VMAP network, and on board R/V *Ron Brown* are used for inversion. Data collected at Kwangju and Yulin seem to be too closely affected by the local sources to be properly represented by the coarse grid size employed in this study. For airborne measurements that span over multiple grid cells during the course of one sampling period, the distribution of the forcing term in the adjoint equation among those grid cells becomes an additional source of uncertainty.

Table 1. Summary of the Observations Considered for This Study

Site/Platform	Location	Sampling Duration	Number of Observations	Cut Point	Use in This Study	Reference
VMAP-Chichijima	27.0°N, 142.2°E	4 hours	165	2.5 μm	assimilation	*Matsumoto et al.* [2003]
VMAP-Hachijo	33.2°N, 139.8°E	4 hours	164	2.5 μm	assimilation	*Matsumoto et al.* [2003]
VMAP-Sado	38.3°N, 138.4°E	4 hours	178	2.5 μm	assimilation	*Matsumoto et al.* [2003]
VMAP-Rishiri	45.1°N, 141.2°E	4 hours	172	2.5 μm	assimilation	*Matsumoto et al.* [2003]
Gosan	33.3°N, 126.2°E	15–30 hours	30	2.5 μm	assimilation	*Schauer et al.* [2003]
Kwangju	35.1°N, 126.5°E	~24 hours	28	2.5 μm	none	*Kim et al.* [2004]
Yulin	38.3°N, 109.7°E	~24 hours	29	2.5 μm	none	*Xu et al.* [2004]
Ron Brown	moving	1–5 hours	118	1.0 μm	assimilation	*Lim et al.* [2003]
C-130	moving	0.4–3 hours	64	1.0 μm	verification	*Huebert et al.* [2004]
Twin Otter	moving	1–5 hours	15	1.0 μm	verification	*Mader et al.* [2002]

Observations made on board the C-130 and Twin Otter aircraft are therefore used for independent evaluation of the inverse modeling and optimization.

5. Results and Discussion

[26] STEM-2k1 is applied to the ACE-Asia domain as the forward model for simulation of BC concentrations and adjoint values during the month of April 2001. Figure 2 shows an example of the predicted spatial distribution of ground-level BC at the time of the maximum simulated concentration during the month of April 2001. Ground-level BC concentrations have a range of 0–5.5 $\mu g/m^3$ during the month, and higher concentrations are simulated in the proximity of the major emission areas of western India and eastern China. BC sources are dominated by the anthropogenic emissions, but the highest concentrations coincide with episodes of significant contributions from BB sources (between 30 and 50% of the total emissions); downwind of major emissions more moderate concentrations are simulated.

[27] The time series of simulated BC concentrations based on the starting emission inventory are compared to the VMAP observations at the four Japanese islands of Chichijima, Hachijo, Sado, and Rishiri (Figures 3a and 3b). In general, the simulations capture the overall behavior and variability of the observations; however, significant differences exist between the simulated and observed concentrations. In particular, there are significant underpredictions at Rishiri and Sado. Similar underpredictions are reported by *Uno et al.* [2003b], who suggest underestimates of Japanese biomass-burning emissions before the rice-planting season as a possible explanation. In their work, the same underlying meteorological model (RAMS) [*Pielke et al.*, 1992] and emission inventory [*Streets et al.*, 2003a] was used, but the model did not include wet removal and assumed zero inflow boundary conditions. The effect of including wet removal in the simulations is also shown in Figures 3a and 3b. Without wet removal the model significantly overestimates BC concentrations at Chichijima and Hachijo. Note that during this period the northern islands of Rishiri and Sado rarely experience heavy precipitation episodes, and therefore inclusion of wet removal has little effect on the BC concentration (and overestimation) at those stations.

[28] VMAP BC measurements provide important information with high temporal resolution and consistency across the stations and therefore form the basis for the current inverse modeling. Figures 4a and 4b show simulated and observed BC concentrations at a few other stations during the ACE-Asia campaign, namely Gosan [*Chuang et al.*, 2003; *Schauer et al.*, 2003], Kwangju [*Kim et al.*, 2004], and Yulin [*Xu et al.*, 2004], as well as aboard R/V *Ron Brown* [*Lim et al.*, 2003]. At Gosan, the simulated BC concentrations are generally lower than the observations. The most significant differences are observed during the periods of yellow sand dust storms (10–13 and 24–27 April). Unexpectedly, during these dust events a large fraction of BC is present in the coarse mode [*Chuang et al.*, 2003]. *Chuang et al.* [2003] associate the coarse mode BC with the coagulation of fine aerosols onto the coarse dust during long-range transport. The simulations presented here, however, do not consider the coagulation processes and should represent all BC concentrations regardless of aerosol size. The measurements at Gosan are deemed among the most reliable BC observations during ACE-Asia, as they were verified by intercomparison with independent side-by-side sampling and analysis. Therefore the underpredictions at Gosan may be a result of underestimated or uninventoried emissions.

[29] Observations at Kwangju and Yulin are grossly underpredicted (Figures 4a and 4b). These two sites are likely close to the local emission sources; the 80 km grid resolution implemented in this study is not capable of resolving concentrations in the vicinity of strong local sources. Because of the large grid size, the same problem, but to a lesser extent, can even exist for VMAP stations. On board the R/V *Ron Brown* the simulated and observed BC concentrations agree more closely (Figure 4b), although the simulation does not consistently reproduce the observed

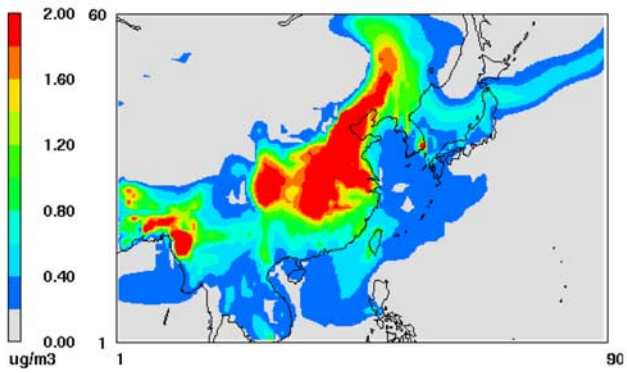

Figure 2. Spatial distributions of BC concentrations at its monthly peak, on 7 April, 0100 UTC.

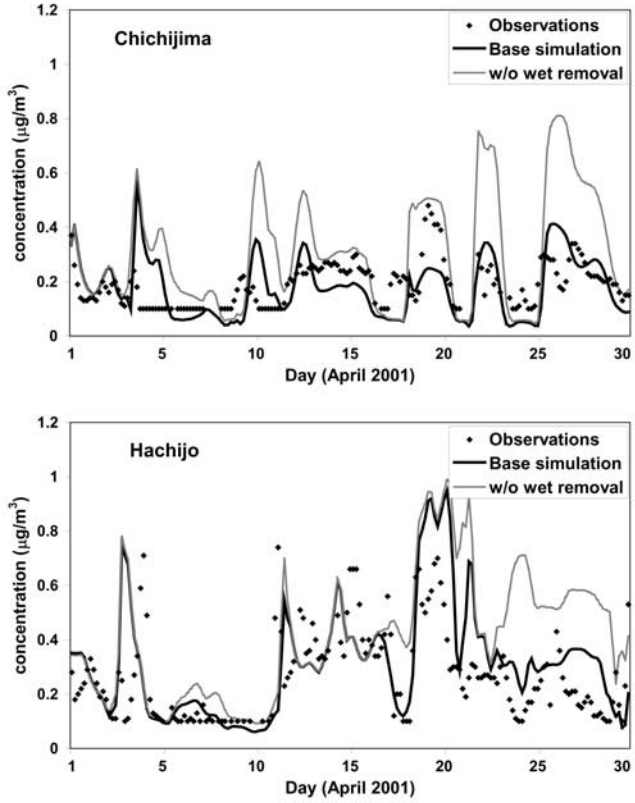

Figure 3a. Time series of BC observed and simulated concentrations at VMAP stations of Chichijima and Hachijo. Gray lines indicate simulation results without wet removal processes.

values. The closer agreement at sea is likely a result of the absence of local sources near the ship.

[30] The adjoint equation is forced (driven) by the discrepancy between the simulated and observed concentrations, at the time and location of the observations. The temporal and spatial distributions of the adjoint variables characterize the areas of influence on the overall objective function; that is, the concentrations and emissions at the locations and times with significant adjoint values (positive or negative) play a more important role in assimilating the observations. The adjoint variable is used to calculate the gradient of the objective function with respect to different input parameters in equation (9). These gradients are the sensitivities of the objective function with respect to various scaling factors in equation (6) at different locations and times. For assimilation of BC, the gradients with respect to initial conditions, boundary conditions, anthropogenic emissions, and biomass-burning emissions are calculated (examples in Figure 5). A negative gradient in Figure 5 indicates that an increased scaling factor is required for the cost function to decrease, and vice versa. Boundary conditions and biomass-burning emissions are represented by their daily gradients, i.e., their values for each day and grid cell are scaled by one scaling factor. For anthropogenic emissions, the scaling factor (for each location and time) is assumed to be composed of a monthly and a daily contribution.

[31] An iterative optimization procedure based on the calculated gradients results in reduced cost function and newly estimated (optimized) scaling factors for different parameters. Unlike data assimilation with simulated observations (the so-called identical twin experiment) in which the cost function can theoretically be reduced to zero, using actual data generally does not result in dramatic reductions in the cost function. Daily averaging of the gradients and applying a single monthly factor for the anthropogenic emissions further constrain the optimization problem and contribute to the modest reduction in the cost function.

[32] The objective function in equation (9) is composed of two parts: one accounting for the distance between the observations and simulations (prediction error), the other for the deviation of the optimized parameters from their background or initial values (assimilation error). The cost associated with each individual observation or scaled parameter is, in part, weighted by the uncertainty assigned to it. In other words, the observations with lower uncertainty account for a larger fraction of the total cost and are more aggressively assimilated. Likewise, input parameters with larger uncertainties are scaled more aggressively, and vice versa. Here, we assign generic uncertainties of 30, 10, and 20% to the observations made at the VMAP stations, Gosan, and on board R/V *Ron Brown*, respectively. These uncertainties should be regarded as ensemble measures of the importance ascribed to each data set on the basis of reliability of the observations and representativeness of the station. For background values we assign uncertainties of

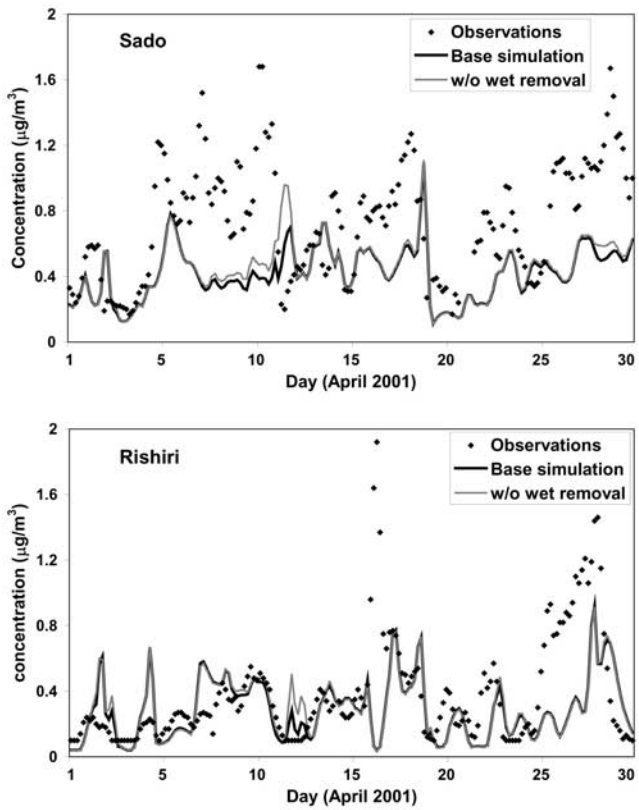

Figure 3b. Time series of BC observed and simulated concentrations at VMAP stations of Sado and Rishiri. Gray lines indicate simulation results without wet removal processes.

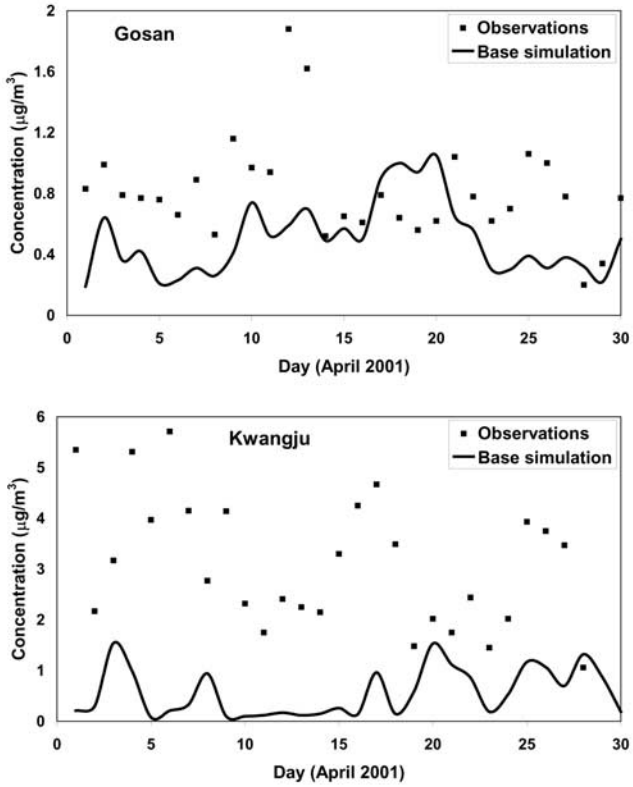

Figure 4a. Observed and simulated BC concentrations at Gosan and Kwangju, Korea.

300, 2000, 500, and 500% to the initial conditions, boundary conditions, biomass burning, and anthropogenic emissions of BC, respectively. The domain-wide uncertainties assigned for the emissions are in line with those reported by *Streets et al.* [2003a], noting that day- and location-specific emissions uncertainties are likely to be higher than those reported for annual and regional estimates. For BB and anthropogenic emissions these domain-wide values are adjusted on the basis of the reported regional uncertainties [*Streets et al.*, 2003a]. Boundary conditions are treated as highly uncertain, as for each specific day and location they may be significantly different from the time- and location-independent background value.

[33] Apart from the uncertainties, the observation- and the background-driven parts of the objective function can be weighted by a global factor, i.e., μ in equation (9). Such weight factor, albeit subjective in nature, can be interpreted as a measure of the strength of the constraints that are applied to the input parameters. The effect of this global factor on the overall assimilation is shown in Figure 6, where the reductions in total square errors or prediction error (observation-driven portion of the objective function) are given for different levels of constraints in the background values. As expected, less constrained cases show larger reductions. On the other hand, the unconstrained assimilation also leads to unrealistically aggressive scaling of the input parameters and therefore larger assimilation errors (Figure 6). An example of this effect can be seen in Figure 7, where the monthly scaling factors for anthropogenic emissions of BC (for three of the cases in Figure 6 and the unconstrained assimilation) are shown. For this study a suitable range of the values for the global weighting factor can be identified as 25–60 on the basis of Figure 6. Within this range the choice of the global weighting factor has little effect on the overall assimilation, as all values result in reasonable reduction in the simulation errors and realistic estimates of the input parameters. We use the conservative end of this range (μ = 25) for the final assimilation that results in approximately 62% reduction in the prediction error.

[34] Spatial distributions of the optimized scaling factors for the initial conditions (as well as the base case initial concentrations) are shown in Figure 8. Scaling initial conditions is likely to have a small effect on the overall cost function, as after the first few days the effect of the initial values disappears. However, the initial concentrations can be important in assimilating the first few days of observations. As expected, the initial concentrations are mostly changed within a few days distance (travel time) from the observation sites, although slight scaling is seen as far as Myanmar.

[35] The most significant change among the optimized parameters is applied to the monthly scaling factors for anthropogenic emissions (Figure 8d), where the magnitudes of those emissions are scaled as far as western India. The scaling is more significant in areas of heavy emissions (Figure 8c), as these areas most significantly influence the objective function. The main feature of the estimated emission field is the reduction in southeastern China, and to lesser extent increased emissions in Japan, northeastern

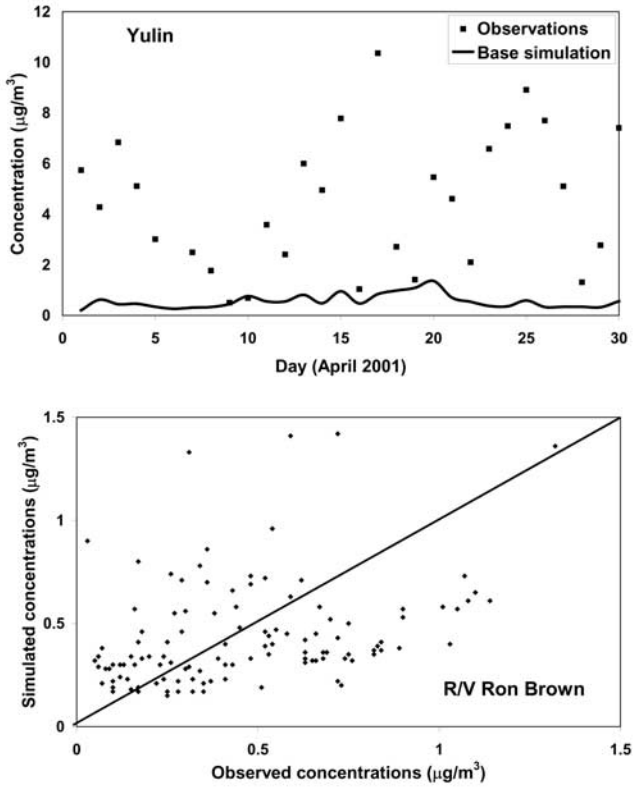

Figure 4b. Observed and simulated BC concentrations at Yulin, China, and on board the R/V *Ron Brown*.

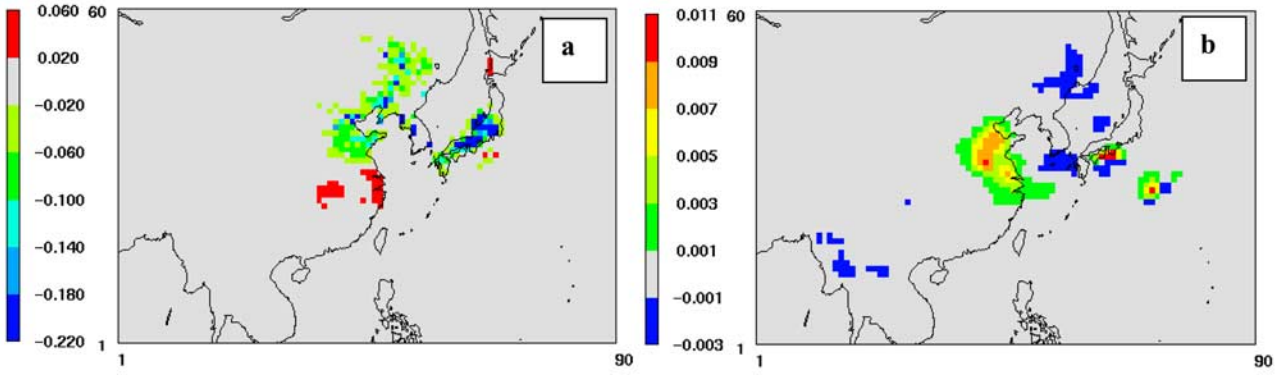

Figure 5. Spatial distributions of the gradient of the objective function with respect to (a) monthly scaling factor for BC anthropogenic emissions and (b) BC initial concentrations. The gradients shown are calculated from the base simulation results, as they change after each iteration.

and eastern China. As the adjoints are integrated backward in time and space from the observation sites, one can consider the adjoints as an ensemble of all back trajectories from the observation sites. Therefore significant adjoint values, gradients, and scaling are more likely to occur in areas in the vicinity of observation sites.

[36] Scales shown in Figures 8b and 8d are for the first vertical layer (surface level). Table 2 gives a summary of the number of cells with significant scaling factors for different parameters and different vertical layers. Monthly anthropogenic emissions and initial conditions scaling factors are assigned a single value for each grid cell over the month, but scaling factors for boundary conditions and biomass-burning emissions are adjusted daily. Overall, only a small fraction of the grid cells experience significant (larger than 10%) change from the starting point of unit scale factors; that fraction for initial conditions, boundary conditions, anthropogenic emissions, and biomass-burning emissions amounts to 0.75, 1.69, 10.9, and 0.07%, respectively. The small fraction of the changed values is due to the constraint that is applied to the optimization. Anthropogenic emissions and boundary conditions undergo the most significant scaling. Biomass-burning emissions are sporadic in nature, and consequently are scaled for the smallest fraction of grid cells. First layer boundary inflow is less likely to affect the cells deep inside the domain, and, as expected, boundary conditions are adjusted more often and more significantly in the higher layers. The largest scaling for boundary conditions occurs in layers 4–12, corresponding to approximately 1–3 km altitude. For the anthropogenic emissions (injected into layers 1–4 only), the first layer is the most significant. From a domain-wide point of view and on an average basis, anthropogenic and biomass-burning emissions tend to be reduced as a result of the optimization, while the initial and boundary conditions are increased.

[37] Apart from the domain-wide averages, a closer look at the smaller regions in the modeling domain provides better insight into the behavior of estimated scaling factors. Figures 9 and 10 show time series of the scaling factors for the average regional emissions (anthropogenic and biomass burning) and lateral boundary conditions (layers 1, 4, 8, and 12). For the boundary conditions, the effect of the southern boundary is insignificant, as it is predominantly one of outflow. Even though the western boundary is very far from the observation sites, it is scaled at higher altitudes. The eastern and northern boundaries exert larger effect on the observation sites and have more significant scaling factors, particularly in the higher layers. The last period of large scaling factors in the northern boundary (days 21–25) coincides with the reported wildfires in Siberia.

[38] On the country level, anthropogenic scaling factors (Figure 10) are generally larger than those associated with biomass-burning emissions. The Philippines and Vietnam/Thailand/Cambodia/Laos region do not have significantly modified emissions. The anthropogenic emissions in southeastern China are consistently and significantly reduced in the optimization process, while those for northeastern China generally exceed unity. For Japan the overall regional scaling factors for anthropogenic emissions indicate an increase; however, some areas on the northern island of Hokkaido show decreased emissions (see Figure 8d). Emissions in Western India/Bangladesh and Korean peninsula remain relatively unchanged. Table 3 shows the total monthly emissions from these subregions. Despite some significant daily scaling factors, the biomass-burning

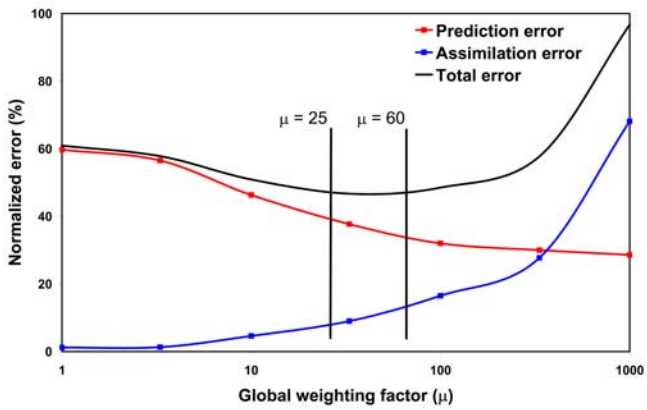

Figure 6. Effect of the global weighting factor, μ in equation (6), on the prediction and background components of cost function. The prediction error is normalized to the error in the base case simulation. The assimilation error is normalized to that of the unconstrained assimilation.

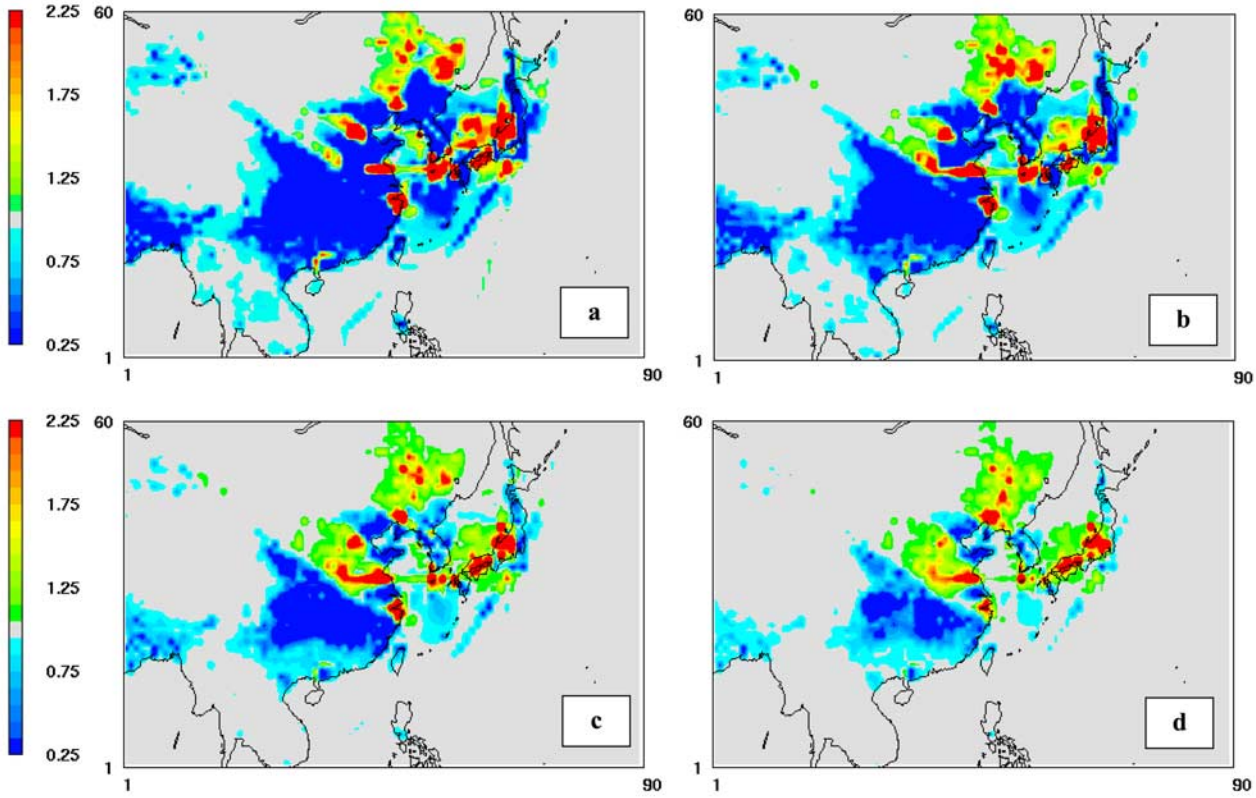

Figure 7. Spatial distributions of the monthly scaling factor for the anthropogenic emissions of BC for different constraint levels in the optimization process: (a) unconstrained, (b) $\mu = 1000$, (c) $\mu = 100$, and (d) $\mu = 10$.

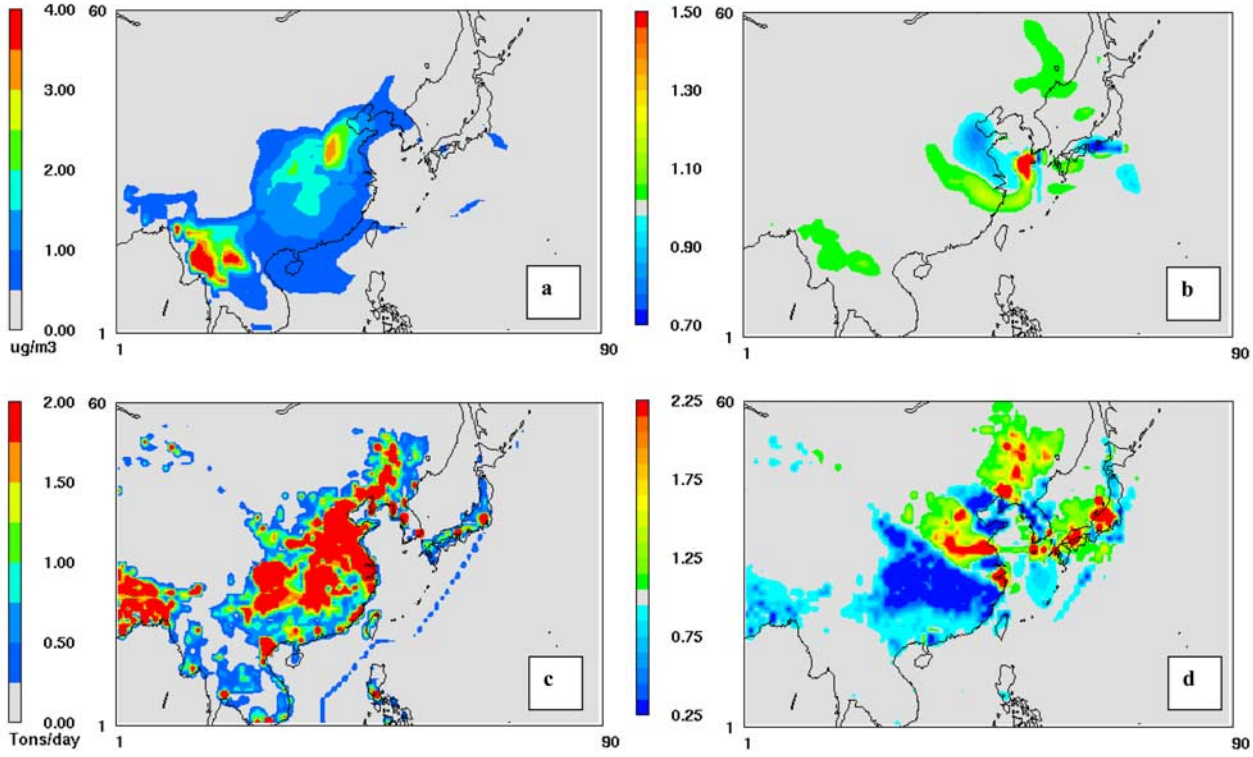

Figure 8. Spatial distribution of the (surface-level) scaling factors for BC initial concentrations (Figure 8b) and monthly BC anthropogenic emissions (Figure 8d). Also shown are the starting (base case) initial conditions (Figure 8a) and ground-level anthropogenic emissions (Figure 8c).

Table 2. Distribution of Significant Scaling Factors in Different Vertical Layers[a]

	Percentage of Cells					
	<0.5	0.5–0.75	0.75–0.9	1.1–1.5	1.5–2.5	>2.5
Anthropogenic Emissions						
Layer 1	4.57	2.17	4.00	3.98	1.76	0.8
Layers 2–4	1.32	1.56	2.69	2.60	0.55	0.13
Layers 5–8	0	0	0	0	0	0
Layers 9–12	0	0	0	0	0	0
Biomass-Burning Emissions						
Layer 1	0.01	0.01	0.08	0.03	0	0
Layers 2–4	0.01	0.01	0.06	0.03	0	0
Layers 5–8	0.01	0	0.04	0.02	0	0
Layers 9–12	0	0	0.01	0	0	0
Boundary Conditions						
Layer 1	0	0	0.10	0.34	0.11	0
Layers 2–4	0.02	0.06	0.17	0.45	0.16	0.05
Layers 5–8	0.07	0.12	0.29	0.72	0.28	0.12
Layers 9–18	0.20	0.34	0.84	0.82	0.30	0.15
Initial Conditions						
Layer 1	0	0.13	0.69	0.70	0.13	0.02
Layers 2–4	0.01	0.17	0.61	0.83	0.14	0.03
Layers 5–8	0.01	0.13	0.25	0.94	0.10	0.02
Layers 9–18	0	0	0	0	0	0

[a]Values are given in percent.

emissions do not change significantly as a result of assimilation. The total domain-wide anthropogenic emissions do not change significantly either; however, some notable changes at the country/subregional levels are seen. It should be noted that the anthropogenic scaling factors are specific to the month of April 2001, and they may reflect an inaccuracy in the predicted seasonality for the emissions rather than one in the inventoried annual emissions.

[39] In general, the increased emissions in different parts of the domain (particularly northeastern and eastern China)

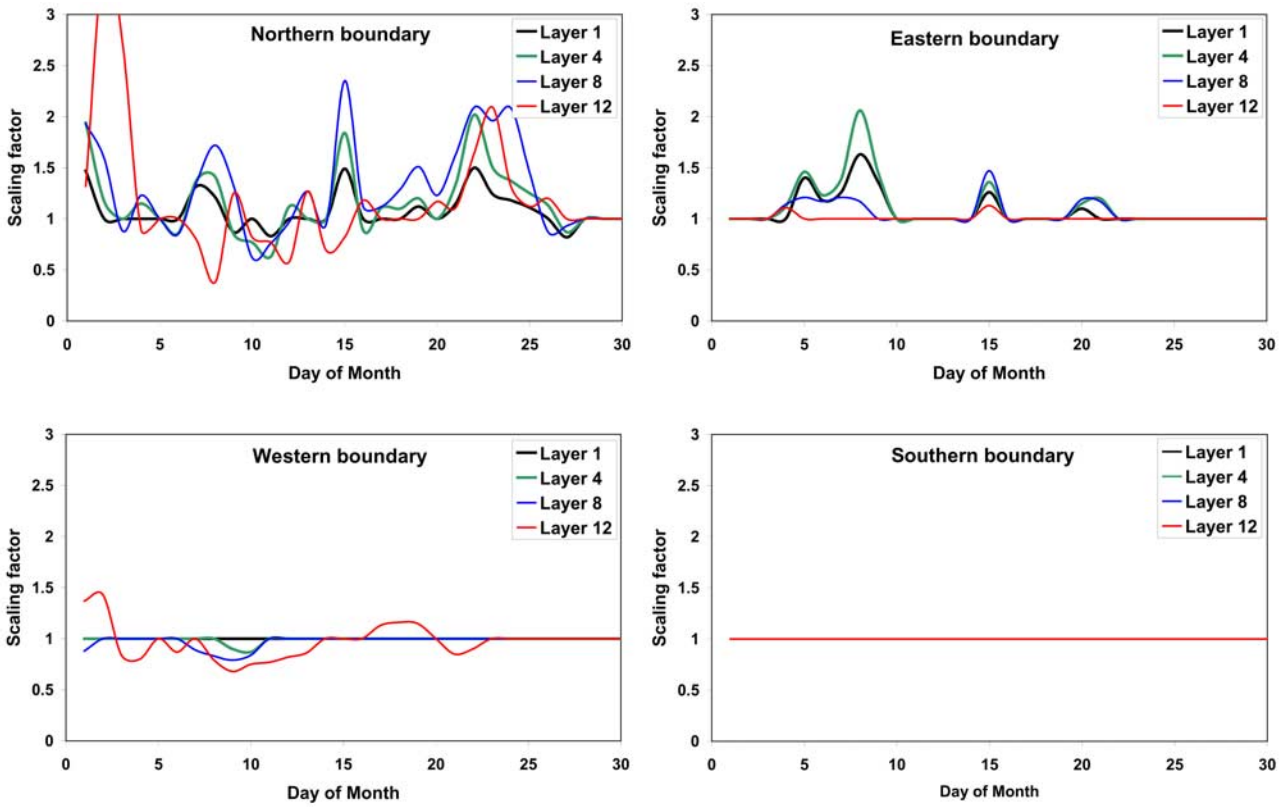

Figure 9. Time series of the scaling factors for BC lateral boundary concentrations (different vertical layers). Only grid cells with scaling factors that are significantly (>10%) different than 1 are used in the averaging.

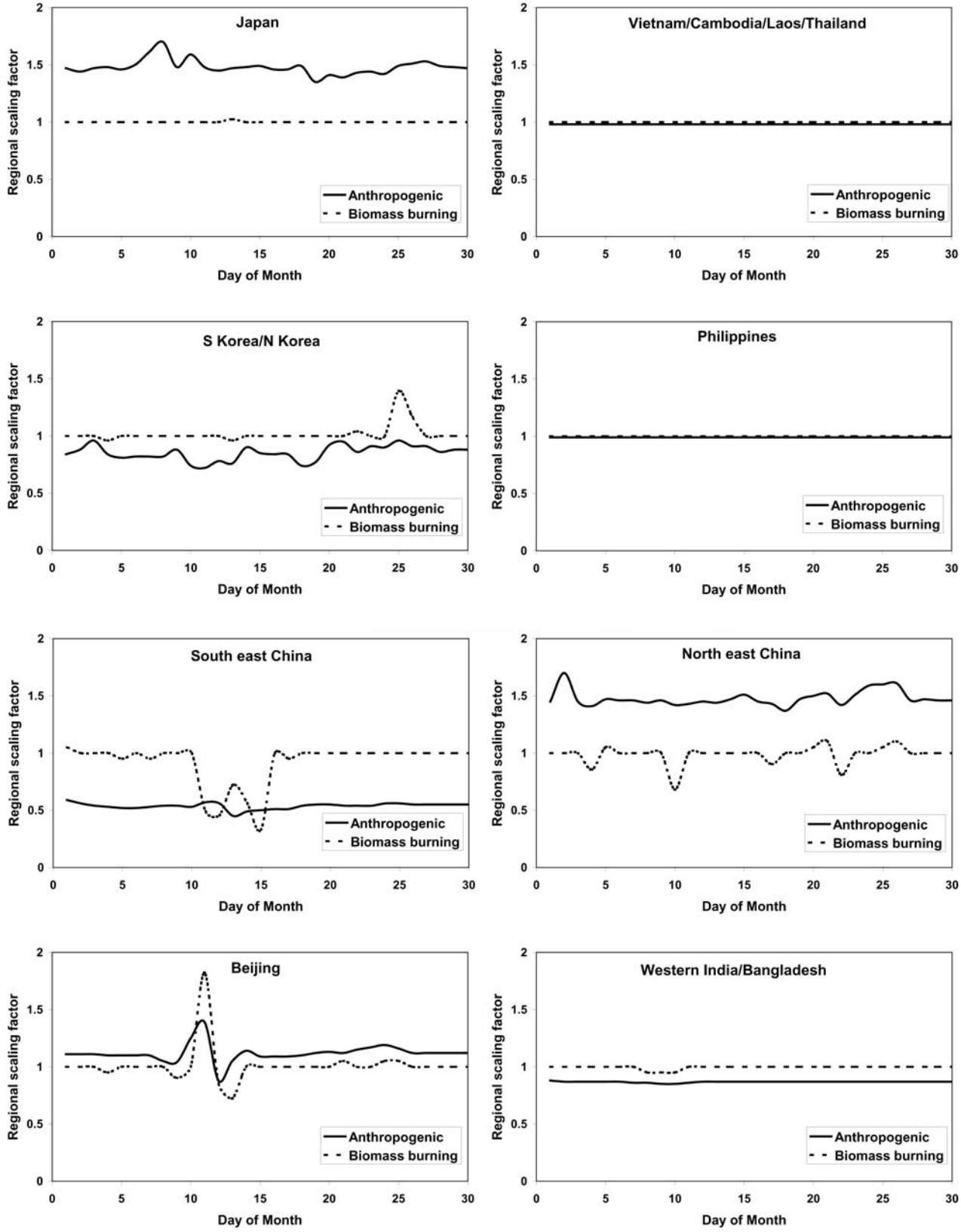

Figure 10. Time series of the scaling factors for BC daily emissions in various regions of the computational domain.

Table 3. Total Anthropogenic and Biomass-Burning Emissions of BC for the Month of April 2001, in Base Case and Optimized Inventories[a]

Region	Anthropogenic Emissions		Biomass-Burning Emissions	
	Base Case	Assimilated	Base Case	Assimilated
Japan	3.16	5.53	0.04	0.03
Vietnam/Laos/Cambodia/Thailand	7.18	6.62	8.69	8.66
North Korea/South Korea	3.19	2.53	0.11	0.11
Philippines	1.10	1.05	0.15	0.15
Southeastern China	28.51	15.63	1.78	1.40
Northeastern China	7.48	13.02	0.99	0.98
Eastern China/Beijing	18.57	20.80	0.99	0.99
Western India/Bangladesh	16.14	11.40	4.70	4.67
Other	26.54	31.76	14.50	14.47
Total	111.87	108.76	31.95	31.46

[a]Values are given in gigagrams.

are in accordance with the findings from other modeling studies of the emissions of BC and other correlated species [*Carmichael et al.*, 2003a; *Tan et al.*, 2004; *Palmer et al.*, 2003; *Allen et al.*, 2004]. Reduced emissions in southeast China, however, are rather unexpected. Among various species, CO concentrations are most closely correlated to those of BC. *Heald et al.* [2004] use aircraft measurements and satellite observations during the TRACE-P campaign for global CO inversion. Their a posteriori estimates for Asian sources of CO are fairly compatible with those found in this study for BC.

[40] Apart from the limitations arising from scarcity of the observations, two potential sources of error can contribute to the reduced emissions in southeast China. First, the meteorological model used in this study generally underestimates the precipitation events [*Uno et al.*, 2003b]. Such underpredictions (more importantly, those events missed altogether by the model) cause model overestimates of BC concentrations, and consequently lead to inaccurate reductions in the emissions as a result of the assimilation process. Second, BC samples used in this study have a cut point of 1 μm or 2.5 μm. Assimilations are carried out on the basis of the premise that all BC is present in the fine mode, while in reality some may be mixed with other aerosol species in the coarse mode. Coarse-mode BC was observed mostly during dust events [*Chuang et al.*, 2003]. The model accounts for all BC emissions regardless of size and therefore may overestimate the sampled BC by the amount of the coarse mode fraction. Albeit small, these overestimates lead to emission reductions in the assimilation that are artifacts.

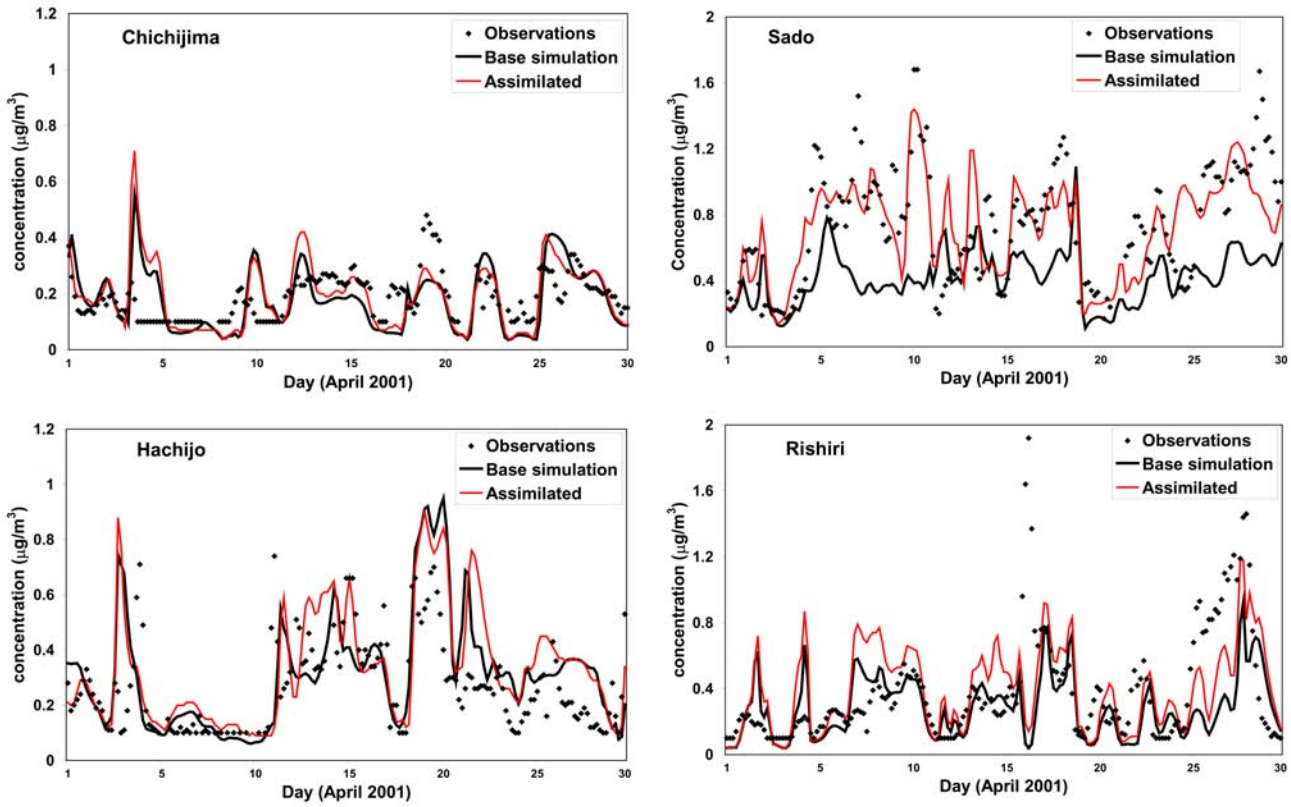

Figure 11a. Assimilated BC concentrations at the VMAP stations.

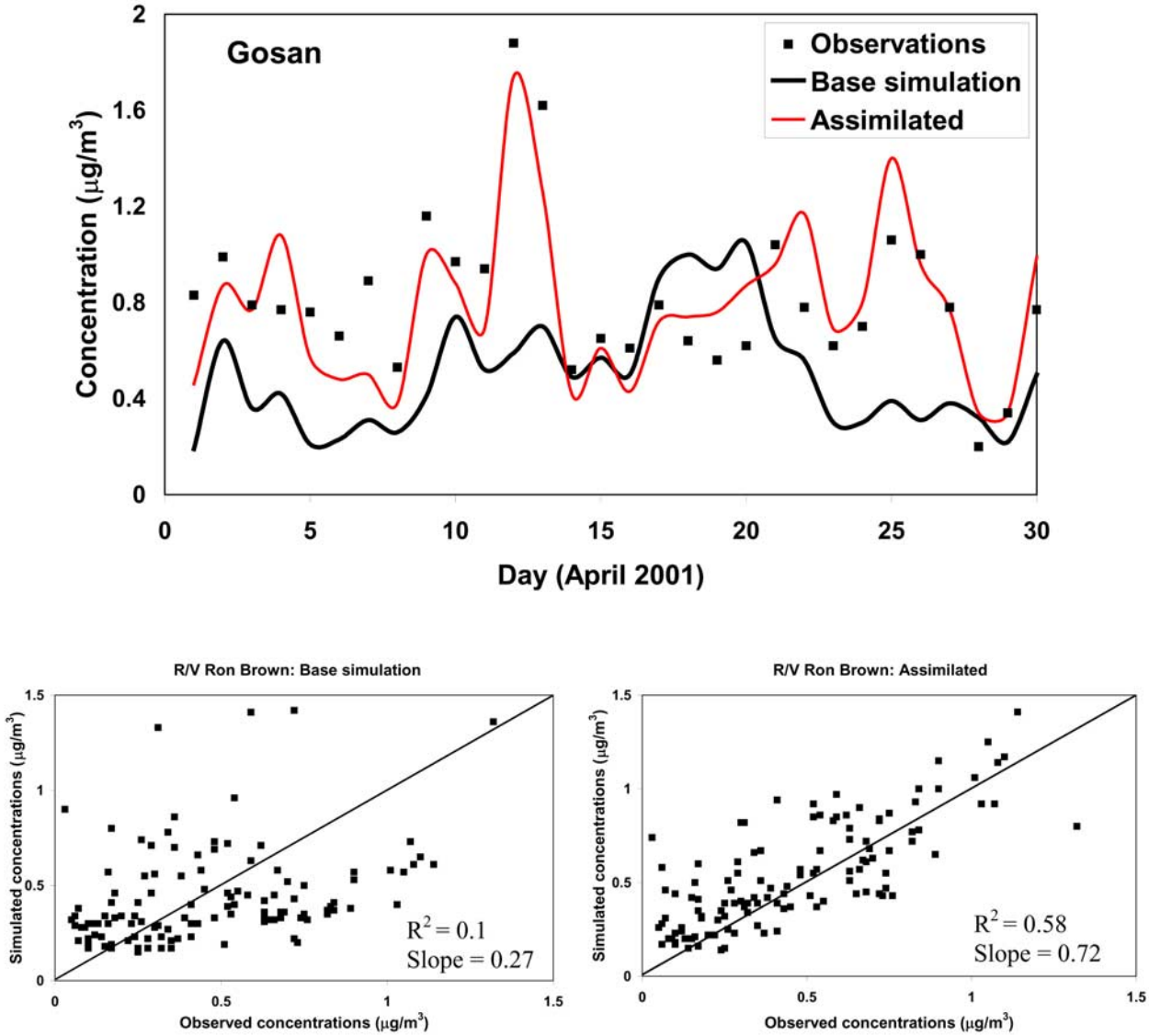

Figure 11b. Assimilated BC concentrations at Gosan and on board the R/V *Ron Brown*.

[41] The scaling and optimization reduces the cost function by pushing the simulations closer to the observations, as shown in Figures 11a and 11b. At different stations and over the course of assimilation, some of the features of the observational time series are successfully reproduced in the simulations. Most notably, model underpredictions at Sado are well compensated. However, some of the discrepancies between the observations and modeled concentrations (particularly at Hachijo and Chichijima) remain relatively unaffected by the optimization and scaling of the parameters. Note that compensating for the errors at one location may drive the simulations further from the observations at another, as seen in some instances in Figures 11a and 11b (e.g., at Rishiri). Such cases are more likely to occur at the VMAP stations, as those observations are assigned higher uncertainties. As expected the observations at Gosan and on board R/V *Ron Brown* are assimilated fairly well, as they are assigned lower uncertainties.

[42] It is desirable to evaluate the assimilation results with observations that were not used in the assimilation. We use the BC measurements on board the C-130 and Twin Otter aircraft in this regard (Figure 12). In case of the C-130, both base case and assimilated simulations grossly underpredict the observations. Moreover, C-130 BC observations are significantly higher than other comparable observations made during the campaign [*Huebert et al.*, 2004]. Highest concentrations are observed during very short sampling periods (10–30 min), likely indicative of passage through polluted air masses. Once again, because of the grid size (80 km) such concentrated plumes are not properly resolved in the simulations. Even though the simulations significantly underpredict the observed values on board the C-130, the assimilated results are in general higher (and therefore closer to the observations), particularly during the periods of highest observed BC concentrations. In other words, the assimilation seems to move the simulation results in the

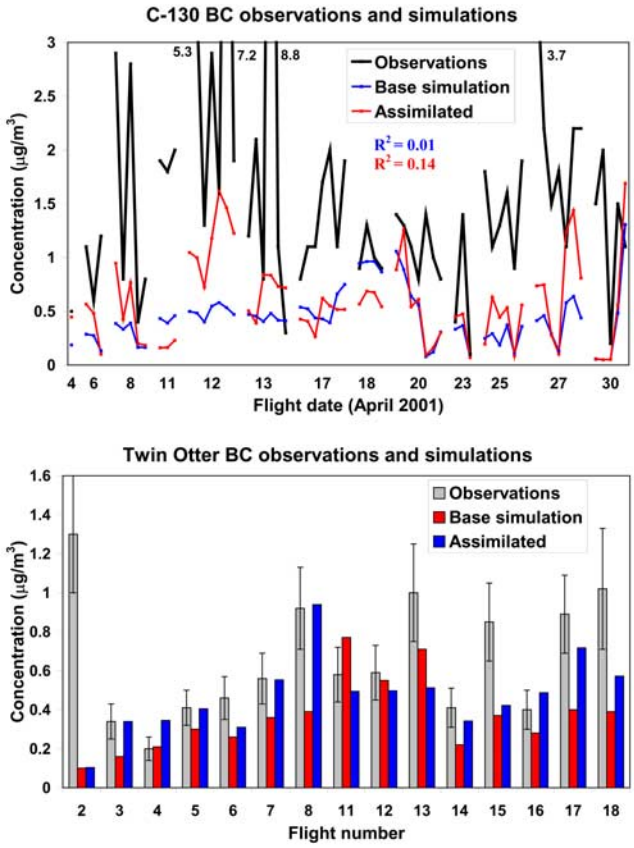

Figure 12. Comparison of the base case and assimilated BC concentrations with airborne measurements.

right direction. The BC measurements on board the Twin Otter are significantly lower than the C-130 observations and show better agreement with the simulations. Note that Twin Otter had three modes for BC sampling, and therefore overlapping samples were taken during each flight [*Mader et al.*, 2002]. Here, we use one sample/measurement for each flight, trying to avoid short sampling periods and pollution plumes (usually the same). Also, some of the reported BC concentrations are below the method's detection limit; in case of two such observations, the lower value is used. The assimilated results are generally in better agreement with the observations. Out of 15 flights, the base case simulation is within the range of uncertainty for 2 observations, as compared to 9 for assimilated results.

[43] It is important to note that the discrepancies between the observations and simulations may be caused by inaccuracies in parameters that are not included in the inverse modeling, e.g., different removal processes or uninventoried emissions. However, the single most plausible source of inaccuracy (apart from those addressed in the assimilation) is the meteorological input (in particular the wind fields) into the simulation. For instance, if the wind field incorrectly predicts that an air mass reaching a station does not cross the boundary or pass over major emission areas, the optimization will not properly assimilate that specific observation. For these reasons, the assimilation and the resulting scaling factors should be regarded as only trend indicators rather than strictly as revised values in the base case emissions inventory (or other input parameters). Furthermore, no uncertainty value or confidence interval has been assigned to the estimated scaling factors; in the absence of such consideration for uncertainties, the results are intended to be treated semiquantitatively.

6. Summary

[44] In this paper, we apply adjoint inverse modeling for the recovery of BC emissions and initial and boundary conditions from observations during ACE-Asia. Measurements at four stations in the VMAP network, at Gosan, South Korea, on board R/V *Ron Brown* and C-130 and Twin Otter aircraft, are chosen as the basis for the evaluation of the forward model, inverse modeling, and verification of the assimilated results. Optimizing location-dependent scaling factors for different input parameters through adjoint inverse modeling significantly reduces the discrepancy between the model predictions and observations. After assimilation, main temporal features at different stations are successfully reproduced by the model. Among different stations, assimilation is more successful for Sado, Gosan, and R/V *Ron Brown*. The assimilated concentrations show markedly better agreement with the measurements made on board the Twin Otter aircraft, and are generally in the direction of improved agreement with C-130 observations.

[45] The assimilation results show that the northern and eastern boundary concentrations, particularly those in mid-altitudes, affect the simulated BC concentrations at the observation sites. Among the different types of parameters estimated, BC anthropogenic emissions have the most significant effect on the overall objective function and therefore change most during the course of the optimization. These emissions are also changed more significantly in the course of assimilation. Total anthropogenic or biomass-burning BC emissions does not change noticeably as a result of assimilation. However, important changes to the anthropogenic BC emissions are seen at the subregional level; notably emissions increase for Japan and northeastern China, and sizable decrease for southeastern China. One can conclude that China in general and its southeastern provinces in particular, are the main areas where further work on emission inventory is required.

[46] Adjoint inverse modeling is a powerful tool for providing insight into constraining various underlying inputs for CTMs. However, reliable and representative data and wide temporal and spatial coverage of measurements are essential for conclusiveness of the inversion. Despite the range of observations during the ACE-Asia field campaign, and because of the size of the eastern Asia region, the scarcity of available and applicable BC observations during ACE-Asia limits the range of conclusions that can be drawn from inverse modeling of this region. Nevertheless, the results from inverse modeling contain important information (in particular about the emissions inventory) that can help better understand the BC distributions in the region.

[47] **Acknowledgment.** This work was supported by National Science Foundation award NSF ITR AP&IM 0205198.

References

Allen, D., K. Pickering, and M. Fox-Rabinovitz (2004), Evaluation of pollutant outflow and CO sources during TRACE-P using model-

calculated, aircraft-based, and Measurements of Pollution in the Troposphere (MOPITT)-derived CO concentrations, *J. Geophys. Res.*, *109*, D15S03, doi:10.1029/2003JD004250.

Bond, T. C., D. G. Streets, K. F. Yarber, S. M. Nelson, J.-H. Woo, and Z. Klimont (2004), A technology-based global inventory of black and organic carbon emissions from combustion, *J. Geophys. Res.*, *109*, D14203, doi:10.1029/2003JD003697.

Byrd, R., P. Lu, and J. Nocedal (1995), A limited memory algorithm for bound constrained optimization, *SIAM J. Sci. Stat. Comput.*, *16*(5), 1190–1208.

Cacuci, D. G. (1981), Sensitivity theory for nonlinear systems. I. Nonlinear functional analysis approach, *J. Math. Phys. N.Y.*, *22*(12), 2794–2802.

Carmichael, G. R., et al. (2003a), Evaluating regional emission estimates using the TRACE-P observations, *J. Geophys. Res.*, *108*(D21), 8810, doi:10.1029/2002JD003116.

Carmichael, G. R., et al. (2003b), Regional-scale chemical transport modeling in support of the analysis of observations obtained during the TRACE-P experiment, *J. Geophys. Res.*, *108*(D21), 8823, doi:10.1029/2002JD003117.

Chuang, P. Y., R. Duvall, M. Bae, A. Jefferson, J. Schauer, H. Yang, J. Yu, and J. Kim (2003), Observations of elemental carbon and absorption during ACE-Asia and implications for aerosol radiative properties and climate forcing, *J. Geophys. Res.*, *108*(D23), 8634, doi:10.1029/2002JD003254.

Chung, S. H., and J. H. Seinfeld (2002), Global distribution and climate forcing of carbonaceous aerosols, *J. Geophys. Res.*, *107*(D19), 4407, doi:10.1029/2001JD001397.

Clarke, A. D., et al. (2004), Size distributions and mixtures of dust and black carbon aerosol in Asian outflow: Physiochemistry and optical properties, *J. Geophys. Res.*, *109*, D15S09, doi:10.1029/2003JD004378.

Cooke, W. F., and J. J. N. Wilson (1996), A global black carbon aerosol model, *J. Geophys. Res.*, *101*, 19,395–19,409.

Cooke, W. F., C. Liousse, H. Cachier, and J. Feichter (1999), Construction of a $1^\circ \times 1^\circ$ fossil fuel emission data set for carbonaceous aerosol and implementation and radiative impact in the ECHAM4 model, *J. Geophys. Res.*, *104*, 22,137–22,162.

Courtier, P., and O. Talagrand (1987), Variational assimilation of meteorological observations with the adjoint of the vorticity equations: Part II. Numerical results, *Q. J. R. Meteorol. Soc.*, *113*, 1311–1328.

Elbern, H., and H. Schmidt (1999), A four-dimensional variational chemistry data assimilation scheme for Eulerian chemistry transport modeling, *J. Geophys. Res.*, *104*, 18,583–18,598.

Elbern, H., and H. Schmidt (2001), Ozone episode analysis by four-dimensional variational chemistry data assimilation, *J. Geophys. Res.*, *106*, 3569–3590.

Elbern, H., H. Schmidt, O. Talagrand, and A. Ebel (2000), 4D-variational data assimilation with an adjoint air quality model for emission analysis, *Environ. Modell. Software*, *15*, 539–548.

Haywood, J. M., and V. Ramaswamy (1998), Global sensitivity studies of the direct radiative forcing due to anthropogenic sulfate and black carbon aerosols, *J. Geophys. Res.*, *103*, 6043–6058.

Haywood, J. M., and K. P. Shine (1995), The effect of anthropogenic sulfate and soot aerosol on the clear sky planetary radiation budget, *Geophys. Res. Lett.*, *22*, 603–606.

Haywood, J. M., D. L. Roberts, A. Slingo, J. M. Edwards, and K. P. Shine (1997), General circulation model calculations of the direct radiative forcing by anthropogenic sulphate and fossil-fuel soot aerosols, *J. Clim.*, *10*, 1562–1577.

Heald, C. L., D. J. Jacob, D. B. A. Jones, P. I. Palmer, J. A. Logan, D. G. Streets, G. W. Sachse, J. C. Gille, R. N. Hoffman, and T. Nehrkorn (2004), Comparative inverse analysis of satellite (MOPITT) and aircraft (TRACE-P) observations to estimate Asian sources of carbon monoxide, *J. Geophys. Res.*, *109*, D23306, doi:10.1029/2004JD005185.

Houtekamer, P. L., and H. L. Mitchell (1998), Data assimilation using an ensemble Kalman filter technique, *Mon. Weather Rev.*, *126*(3), 796–811.

Huebert, B. J., T. Bates, P. B. Russell, G. Shi, Y. J. Kim, K. Kawamura, G. Carmichael, and T. Nakajima (2003), An overview of ACE-Asia: Strategies for quantifying the relationships between Asian aerosols and their climatic impacts, *J. Geophys. Res.*, *108*(D23), 8633, doi:10.1029/2003JD003550.

Huebert, B., T. Bertram, J. Kline, S. Howell, D. Eatough, and B. Blomquist (2004), Measurements of organic and elemental carbon in Asian outflow during ACE-Asia from the NSF/NCAR C-130, *J. Geophys. Res.*, *109*, D19S11, doi:10.1029/2004JD004700.

Jacob, D. J., J. H. Crawford, M. M. Kleb, V. S. Connors, R. J. Bendura, J. L. Raper, G. W. Sachse, J. C. Gille, L. Emmons, and C. L. Heald (2003), Transport and Chemical Evolution Over the Pacific (TRACE-P) aircraft mission: Design, execution, and first results, *J. Geophys. Res.*, *108*(D20), 9000, doi:10.1029/2002JD003276.

Jacobson, M. Z. (1998), *Fundamentals of Atmospheric Modeling*, Cambridge Univ. Press, New York.

Jacobson, M. Z. (2001), Strong radiative heating due to the mixing state of black carbon in atmospheric aerosols, *Nature*, *409*, 695–697.

Jacobson, M. Z. (2002), Control of fossil-fuel particulate black carbon and organic matter, possibly the most effective method of slowing global warming, *J. Geophys. Res.*, *107*(D19), 4410, doi:10.1029/2001JD001376.

Khattatov, B., J.-F. Lamarque, L. V. Lyjak, R. Menard, P. Levelt, X. Tie, G. P. Brasseur, and J. C. Gille (2000), Assimilation of satellite observations of long-lived chemical species in global chemistry-transport models, *J. Geophys. Res.*, *105*, 29,135–29,144.

Kim, K. W., Z. He, and Y. J. Kim (2004), Physicochemical characteristics and radiative properties of Asian dust particles observed at Kwangju, Korea, during the 2001 ACE-Asia intensive observation period, *J. Geophys. Res.*, *109*, D19S02, doi:10.1029/2003JD003693.

Koch, D. (2001), The transport and direct radiative forcing of carbonaceous and sulfate aerosols in the GISS GCM, *J. Geophys. Res.*, *106*, 20,311–20,332.

Le Dimet, F., and O. Talagrand (1986), Variational algorithms for analysis and assimilation of meteorological observations: Theoretical aspects, *Tellus, Ser. A*, *38*, 97–110.

Lim, H. J., B. J. Turpin, L. M. Russell, and T. S. Bates (2003), Organic and elemental carbon measurements during ACE-Asia suggest a longer atmospheric lifetime for elemental carbon, *Environ. Sci. Technol.*, *37*, 3055–3061.

Liousse, C., J. E. Penner, C. Chuang, J. J. Walton, H. Eddleman, and H. Cachier (1996), A global three-dimensional model study of carbonaceous aerosols, *J. Geophys. Res.*, *101*, 19,411–19,432.

Mader, B. T., R. C. Flagan, and J. H. Seinfeld (2002), Airborne measurements of atmospheric carbonaceous aerosols during ACE-Asia, *J. Geophys. Res.*, *107*(D23), 4704, doi:10.1029/2002JD002221.

Marchuk, G. (1974), *Numerical Solution of the Problems of the Dynamics of the Atmosphere and the Ocean* (in Russian), Gidrometeoizdat, St. Petersburg.

Marchuk, G. (1986), *Mathematical Models in Environmental Problems*, Elsevier, New York.

Matsumoto, K., M. Uematsu, T. Hayano, K. Yoskioka, H. Tanimoto, and T. Iida (2003), Simultaneous measurements of particulate elemental carbon on the ground observation network over the western North Pacific during the ACE-Asia campaign, *J. Geophys. Res.*, *108*(D23), 8635, doi:10.1029/2002JD002744.

Menard, R., S. E. Cohn, L. P. Chang, and P. M. Lyster (2000), Assimilation of stratospheric chemical tracer observations using a Kalman filter. Part I: Formulation, *Mon. Weather Rev.*, *128*(8), 2654–2671.

Menut, L. (2003), Adjoint modeling for atmospheric pollution process sensitivity at regional scale, *J. Geophys. Res.*, *108*(D17), 8562, doi:10.1029/2002JD002549.

Menut, L., R. Vautard, M. Beekmann, and C. Honore (2000), Sensitivity of photochemical pollution using the adjoint of a simplified chemistry-transport model, *J. Geophys. Res.*, *105*, 15,379–15,402.

Miehe, P., A. Sandu, G. R. Carmichael, Y. Tang, and D. Daescu (2002), A communication library for the parallelization of air quality models on structured grids, *Atmos. Environ.*, *36*, 3917–3930.

Mulholland, M., and J. H. Seinfeld (1995), Inverse air pollution modeling of urban-scale carbon monoxide emissions, *Atmos. Environ.*, *29*, 497–516.

Myhre, G., F. Stordal, K. Restad, and I. Isaksen (1998), Estimates of the direct radiative forcing due to sulfate and soot aerosols, *Tellus, Ser. B*, *50*, 463–477.

Navon, I. M. (1997), Practical and theoretical aspects for adjoint parameter estimation and identifiability in meteorology and oceanography, *Dyn. Atmos. Oceans*, *27*, 55–79.

Palmer, P. I., D. J. Jacob, D. B. A. Jones, C. L. Heald, R. M. Yantosca, J. A. Logan, G. W. Sachse, and D. G. Streets (2003), Inverting for emissions of carbon monoxide from Asia using aircraft observations over the western Pacific, *J. Geophys. Res.*, *108*(D21), 8828, doi:10.1029/2003JD003397.

Penner, J. E., C. C. Chuang, and K. Grant (1998), Climate forcing by carbonaceous and sulfate aerosols, *Clim. Dyn.*, *14*, 839–851.

Pielke, R. A., et al. (1992), A comprehensive meteorological modeling system: RAMS, *Meteorol. Atmos. Phys.*, *49*, 69–91.

Sandu, A., D. N. Daescu, and G. R. Carmichael (2003), Direct and adjoint sensitivity analysis of chemical kinetic systems with KPP: Part I: Theory and software tools, *Atmos Environ.*, *37*, 5083–5096.

Sandu, A., D. N. Daescu, G. R. Carmichael, and T. Chai (2005), Adjoint sensitivity analysis of regional air quality models, *J. Comput. Phys.*, *204*, 222–252.

Schaap, M., H. A. C. D. Van Der Gon, F. J. Dentener, A. J. H. Visschedijk, M. Van Loon, H. M. ten Brink, J.-P. Putaud, B. Guillaume, C. Liousse, and P. J. H. Builtjes (2004), Anthropogenic black carbon and fine aerosol

distribution over Europe, *J. Geophys. Res.*, *109*, D18207, doi:10.1029/2003JD004330.

Schauer, J. J., et al. (2003), ACE-Asia intercomparison of a thermal-optical method for the determination of particle-phase organic and elemental carbon, *Environ. Sci. Technol.*, *37*, 993–1001.

Schmidt, H., and D. Martin (2003), Adjoint sensitivity of episodic ozone in the Paris area to emissions on the continental scale, *J. Geophys. Res.*, *108*(D17), 8561, doi:10.1029/2001JD001583.

Seinfeld, J. H., and S. N. Pandis (1998), *Atmospheric Chemistry and Physics: From Air Pollution to Climate Change*, John Wiley, Hoboken, N. J.

Seinfeld, J. H., et al. (2004), Regional climatic and atmospheric chemical effects of Asian dust and pollution, *Bull. Am. Meteorol. Soc.*, *85*(3), 367–380.

Sirkes, Z., and E. Tziperman (1997), Finite difference of adjoint or adjoint of finite difference?, *Mon. Weather Rev.*, *125*(12), 3373–3378.

Streets, D. G., et al. (2003a), An inventory of gaseous and primary aerosol emissions in Asia in the year 2000, *J. Geophys. Res.*, *108*(D21), 8809, doi:10.1029/2002JD003093.

Streets, D. G., K. F. Yarber, J.-H. Woo, and G. R. Carmichael (2003b), Biomass burning in Asia: Annual and seasonal estimates and atmospheric emissions, *Global Biogeochem. Cycles*, *17*(4), 1099, doi:10.1029/2003GB002040.

Talagrand, O. (1981a), A study of the dynamics of four dimensional data assimilation, *Tellus*, *33*, 43–60.

Talagrand, O. (1981b), On the mathematics of data assimilation, *Tellus*, *33*, 321–339.

Talagrand, O., and P. Courtier (1987), Variational assimilation of meteorological observations with the adjoint of the vorticity equations: Part I. Theory, *Q. J. R. Meteorol. Soc.*, *113*, 1311–1328.

Tan, Q., W. L. Chameides, D. Streets, T. Wang, J. Xu, M. Bergin, and J. Woo (2004), An evaluation of TRACE-P emission inventories from China using a regional model and chemical measurements, *J. Geophys. Res.*, *109*, D22305, doi:10.1029/2004JD005071.

Uno, I., et al. (2003a), Regional chemical weather forecasting system CFORS: Model descriptions and analysis of surface observations at Japanese island stations during the ACE-Asia experiment, *J. Geophys. Res.*, *108*(D23), 8668, doi:10.1029/2002JD002845.

Uno, I., G. R. Carmichael, D. Streets, S. Satake, T. Takemura, J.-H. Woo, M. Uematsu, and S. Ohta (2003b), Analysis of surface black carbon distributions during ACE-Asia using a regional-scale aerosol model, *J. Geophys. Res.*, *108*(D23), 8636, doi:10.1029/2002JD003252.

Usbeck, R., R. Schlitzer, G. Fischer, and G. Wefer (2003), Particle fluxes in the ocean: Comparison of sediment trap data with results from inverse modeling, *J. Mar. Syst.*, *39*(3–4), 167–183.

van Loon, M., P. J. H. Builtjes, and A. J. Segers (2000), Data assimilation of ozone in the atmospheric transport chemistry model LOTOS, *Environ. Modell. Software*, *15*, 603–609.

Vautard, R., M. Beekmann, and L. Menut (2000), Applications of adjoint modelling in atmospheric chemistry: Sensitivity and inverse modelling, *Environ. Modell. Software*, *15*, 703–709.

Vukicevic, T., and P. Hess (2000), Analysis of tropospheric transport in the Pacific Basin using the adjoint technique, *J. Geophys. Res.*, *105*, 7213–7230.

Wang, C. (2004), A modeling study on the climate impacts of black carbon aerosols, *J. Geophys. Res.*, *109*, D03106, doi:10.1029/2003JD004084.

Woo, J., et al. (2003), Contribution of biomass and biofuel emissions to trace gas distributions in Asia during the TRACE-P experiment, *J. Geophys. Res.*, *108*(D21), 8812, doi:10.1029/2002JD003200.

Xu, J., M. H. Bergin, R. Greenwald, J. J. Schauer, M. M. Shafer, J. L. Jaffrezo, and G. Aymoz (2004), Aerosol chemical, physical, and radiative characteristics near a desert source region of northwest China during ACE-Asia, *J. Geophys. Res.*, *109*, D19S03, doi:10.1029/2003JD004239.

G. R. Carmichael, T. Chai, and Y. Tang, Center for Global and Regional Environmental Research, University of Iowa, 424 IATL, Iowa City, IA 52242-1297, USA.

A. Hakami, D. K. Henze, and J. H. Seinfeld, Department of Chemical Engineering, California Institute of Technology, 1200 E. California Boulevard, Pasadena, CA 91125, USA. (seinfeld@caltech.edu)

A. Sandu, Department of Computer Science, Virginia Polytechnic Institute and State University, 660 McBryde Hall, Blacksburg, VA 4061, USA.